ACS Photonics

Article

pubs.acs.org/journal/apchd5

Scaling the Response of Nanocrescent Antennas into the Ultraviolet

Miguel Rodriguez,[†] Cynthia Furse,[†] Jennifer S. Shumaker-Parry,[‡] and Steve Blair*[,†]

[†]Department of Electrical and Computer Engineering, University of Utah, 50 South Central Campus Drive, Room 3280, Salt Lake City, Utah 84112, United States

[‡]Department of Chemistry, University of Utah, 315 South 1400 East, Room 2020, Salt Lake City, Utah 84112, United States

ABSTRACT: Fundamental resonance modes of nanocrescent optical antennas are associated with large electric fields at the crescent tips. These antennas have been extensively studied due to their relative ease of fabrication and tunable response via methods such as nanosphere template lithography. To date, investigations have only been performed in the visible to mid-infrared range, where the multimode anisotropic response has been documented both experimentally and through simulations. However, the presence of interband transitions in the dielectric response of the metals used for these studies complicates the analysis of the higher-order resonance modes. In this paper, we perform a comprehensive investigation of the electromagnetic response of aluminum nanocrescent antennas. Aluminum has an interband transition in the near-infrared that facilitates scaling of the resonance modes into the ultraviolet part of the spectrum, thus, allowing investigation of the higher-order modes of the nanocrescent structure. These higher-order modes exhibit intense and controllable hot spots, suggesting that nanocrescent antennas are suited for applications in the UV regime.

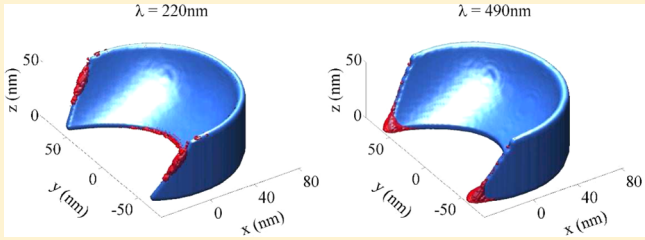

KEYWORDS: *plasmonics, nanoantennas, ultraviolet*

Nanocrescent-shaped antennas have been widely studied.[1−4] The high field-enhancement, combined with ease of fabrication[5,6] and tunability,[7] make these structures very promising for many applications. One of the challenges in scaling antenna resonances to short wavelengths is the dielectric response of the constituent metals. Gold and silver, for example, have interband transitions in the green and blue parts of the spectrum, respectively, and thus limit strong resonance response to longer wavelengths. Therefore, most studies to date of antenna response in the ultraviolet have employed other metals, such as aluminum.[8−17] Another significant issue in scaling antenna response to the ultraviolet range is the physical size of the antenna; the resonance wavelengths of the antenna generally scale with the antenna size,[18] therefore, requiring high-resolution patterning. An alternative is to utilize higher-order antenna modes, which are well-characterized for dipole[13,19] and simple rod[18,20] antennas.

Nanocrescent antennas exhibit a rich spectrum of anisotropic modes,[21] which have only been studied in the visible to mid-infrared. These studies have been based on the use of gold or silver for the antenna, complicating the analysis of the structure of the higher-order modes as the resonance wavelengths of these modes approach the interband transition frequencies of the metals. Aluminum, by contrast, has an interband transition near 800 nm with a Drude-like free-electron response from the visible to UV wavelengths.[22] Even though other metal options exist for UV plasmonics,[22−27] we use aluminum in part due to its compatibility with conventional semiconductor processing.[18]

SIMULATION MODEL

Nanocrescent antennas are fabricated using nanosphere template lithography.[5] The process begins with placing polystyrene beads on a glass substrate to serve as a template for the crescent antennas as shown in Figure 1a. A metal layer is then deposited at a controlled angle, Figure 1b. The thickness can be controlled by adjusting deposition rate and time. The deposition angle θ is defined with respect to the normal to the substrate and can be used to control the top and bottom widths of the antenna. Increasing the deposition angle, for instance, results in a wider antenna at the base and narrower at the top. Deposition is followed by etching at a normal angle to the substrate, Figure 1c. The bead's shadow acts to protect the metal underneath so that only the metal outside of this area is etched. The result is a crescent of height H and diameter D equal to the diameter of the bead used to create it. Finally, the beads are removed by tape-off, leaving only the crescents on the substrate, Figure 1d.

In this study, the nanocrescent response was obtained through simulation using Lumerical's FDTD Solutions, and all data processing was performed using Matlab R2009b. FDTD Solutions allows for objects to be constructed from Boolean combinations of simpler geometrical objects. A crescent on a substrate can be created by overlaying four shapes with priorities, as indicated in Figure 2. The program interprets this as a substrate that overrides anything embedded within it, since it has the highest priority. Similarly, a portion of the right

Received: December 5, 2013
Published: May 29, 2014

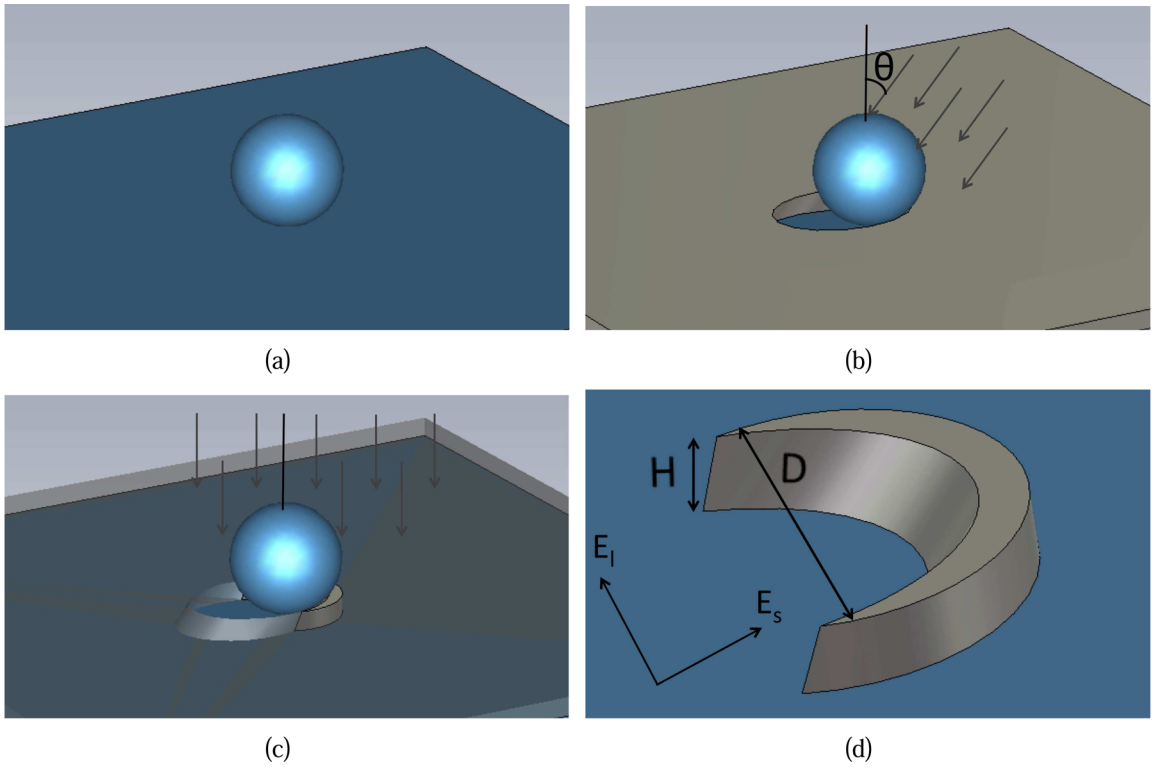

Figure 1. Fabrication of antennas via nanosphere template lithography. (a) The process begins by depositing beads on a substrate. (b) A layer of metal is then deposited at a desired angle. (c) This is followed by etching at a right angle to the substrate where the bead acts to protect the metal beneath it. (d) The bead is then lifted off, leaving a crescent-shaped nanoantenna.

Shape	Material	Priority
Hexahedral	Glass	1
Tilted Cylinder	Free Space	2
Sphere	Free Space	3
Right Cylinder	Aluminum	4

(a)

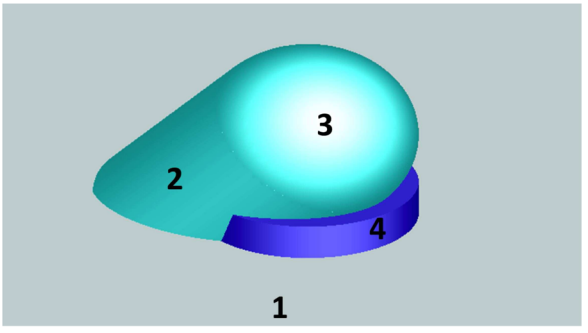

(b)

Figure 2. Priority assigned to different objects in the creation of the crescent simulation model. An object with a lower number overrides higher number objects embedded within it.

cylinder is overridden by the sphere and tilted cylinder, resulting in a crescent shape.

The simulation model described above follows directly from the fabrication process, where the "shadow" of the bead prevents metal from depositing onto certain locations, Figure 1b, and prevents metal from being removed during etching, Figure 1c. Following geometrical model definition, the structure is meshed. FDTD Solutions allows hexahedral meshes where the height, width and length of the hexahedra can be independently defined. The grid resolution is a compromise between accuracy and computational expense. Crescents with diameters 80 nm and less were meshed at $0.5 \times 0.5 \times 0.5$ nm^3 in the x, y, and z directions. Crescents with larger diameters were meshed coarser at $1 \times 1 \times 1$ nm^3 in order to reduce simulation time and storage space.

After defining the mesh, the model was augmented with monitors to record near-field data or power flow for far-field calculations. For near-field calculations, 3-D monitors were used to record electric field intensity. The volume occupied by these monitors is delineated by the yellow lines in Figure 3. The spatial locations where the electric field intensity and materials' properties are determined were also recorded in the monitors and have the same resolution as the enclosed mesh. For far field simulations, the 3-D monitor was replaced by six 2-D power flow monitors to determine absorption cross-section and six additional power flow monitors enclosing the source were added to find the scattering cross-section.

A Total Field Scattered Field (TFSF) source was used for simulations. This type of source is used to simulate plane wave incidence on finite structures. This follows in line with experimental procedures where a nanocrescent is much smaller

dx.doi.org/10.1021/ph400151n | ACS Photonics 2014, 1, 496−506

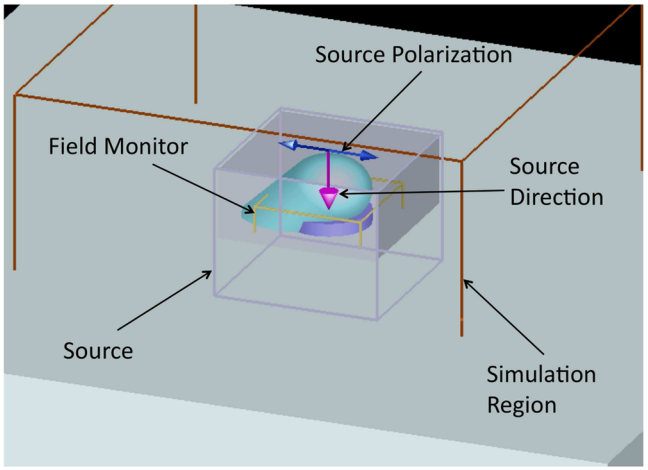

Figure 3. Simulation setup.

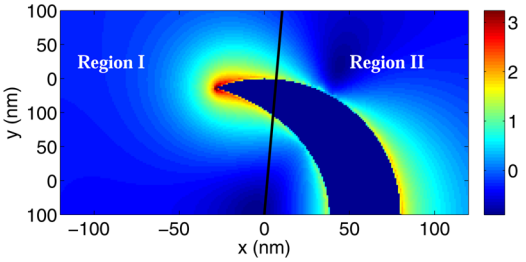

Figure 4. Fields are averaged over Regions I and II to determine the tip and backbone near-field response. Fields are also averaged over both regions combined to determine the overall response.

than the laser beam spot used to characterize it. In Figure 3 this is shown as the volume enclosed by gray lines. The incident direction of the source is indicated by the pink arrow and the electric field polarization by the blue arrows. Polarization can be defined for 360° around the incident axis. The two polarizations of interest are short axis (SA) polarization, E_s, and long axis (LA) polarization, E_l, defined as fields polarized along the short and long axis of the crescent, respectively. This is illustrated in Figure 1d.

After defining the source, the complete structure was enclosed by a simulation region. This region is shown enclosed by brown lines in Figure 3. This simulation region provides perfectly matched layers (PML) boundary conditions to absorb light incident upon it and avoid reflecting it back toward the structure being simulated. The near field response of each crescent was determined from simulations performed at discrete wavelengths in the range of 200 to 600 nm in increments of 10 nm and for each electric field polarization.

Simulation of crescents was followed by data extraction and analysis. As described in ref 28, data from power flow monitors located within and outside of the volume of the TFSF source was extracted to compute the absorption and scattering cross-section, respectively. The extinction cross-section is simply the sum of the two. Near-field data was analyzed by extracting the data from FDTD Solutions and analyzing it using Matlab. The field data values produced by the simulations are in reference to a unit source, and therefore represent field enhancement. In order to better define the usefulness of the crescents, the fields were averaged over a small volume. Only fields in free space were considered for this analysis; fields inside materials were masked by using the index of refraction. In this study, a 1000 nm^3 amorphous volume following the highest field intensity around the crescent was used. For example, assuming a 1 × 1 × 1 nm^3 mesh, each mesh point approximates the field intensity over the 1 nm^3 surrounding the point. In order to represent a 1000 nm^3 volume, 1000 mesh points are needed. This is true regardless of the arrangement of the points. Therefore, the 1000 highest field intensity values (specified at 1000 mesh points) were averaged to determine the near field response. Due to the symmetry of the structure, only one-half of the crescent was analyzed, as shown in Figure 4. The near-field response at the tips was determined by averaging the highest field intensity points in region I of Figure 4. The dividing plane between tip and backbone was selected to be 85° from the *xz*-plane. Similarly, the near-field response at the backbone was determined by averaging the highest field intensity points in region II. The overall crescent response was obtained by averaging over regions I and II combined.

RESULTS

The resulting intensity response in each region for a crescent 160 nm in diameter, 30 nm in height, deposition angle of 40° and excited using a short-axis polarized source is shown in Figure 5a. The figure shows that the largest peak from the tip response and overall crescent response coincide (λ = 530 nm). At this wavelength, the tips produce the dominant contribution to the overall crescent response, as can be seen directly from Figure 5b. This peak is associated with the short-axis dipole resonance, and the wavelength at which it occurs is primarily affected by the diameter of the crescent. The figure shows an additional peak at λ = 270 nm. This peak has comparable contributions from both tip and backbone fields and has a quadrupole character. In previous papers, this resonance has been denoted an "out-of-plane" resonance,[21] which is descriptive based on the charge oscillation along the edges of the tips (in the *z*-direction), resulting in two distinct hot spots at the corners of each tip. We further observe that the wavelength of this peak can be adjusted by changing the deposition angle (which changes the width of the backbone) in addition to the crescent diameter.

Similarly, for a long-axis polarized source, the tip, backbone, and overall responses of the nanocrescent are shown in Figure 6a. Excitation of the crescent with this polarization results in a dipole resonance (which lies outside the range of the graph and is influenced by the interband transition of Al) and a quadrupole resonance (λ = 420 nm). Both of these resonances shift with the crescent diameter, while the quadrupole resonance is also affected by the backbone width. The enhancement spectrum also exhibits multiple higher-order antenna resonances, the dominant one located at λ = 220 nm, which shifts with the width of the crescent backbone. The near-field intensity patterns are illustrated in Figure 6b.

To further analyze the resonance modes of the crescent antenna, a parametric study was performed to determine the effects of diameter, height, and deposition angle. The crescent diameter was varied from 40 to 200 nm in increments of 20 nm, the crescent height was varied from 20 nm to half of the crescent diameter in increments of 10 nm, and the deposition angle was varied from 20 to 60° in increments of 10°.

Scaling with Crescent Diameter. Figure 7 shows the crescent's response as the diameter varies. The results show that decreasing the diameter of the nanocrescent has the effect of blue shifting the dipole and quadrupole resonances, as

dx.doi.org/10.1021/ph400151n | ACS Photonics 2014, 1, 496−506

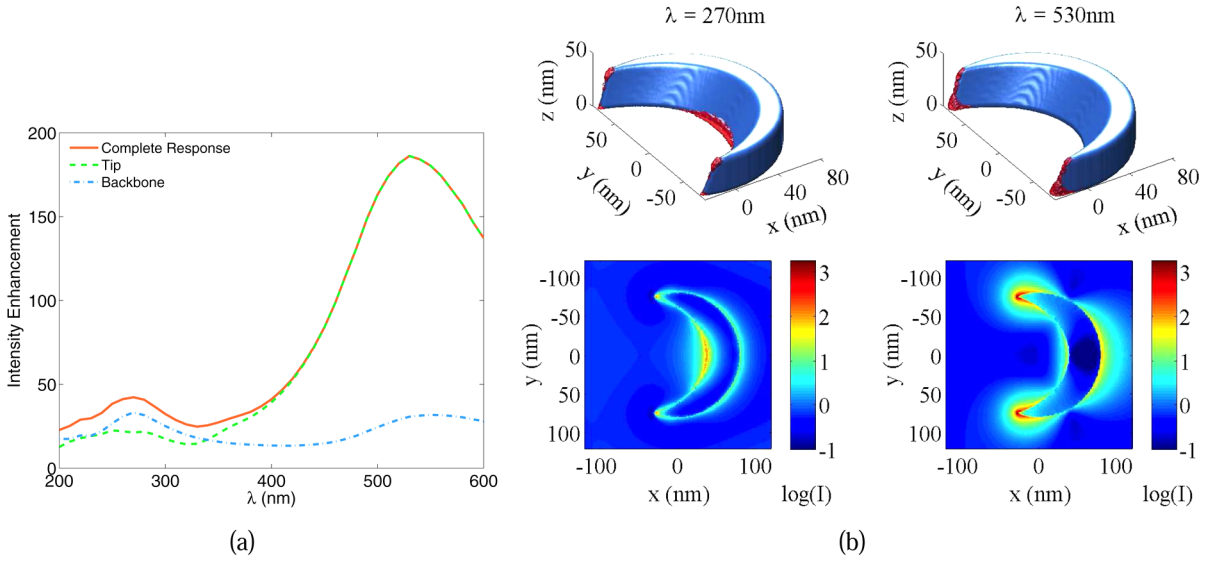

Figure 5. (a) Intensity enhancement response of a crescent antenna with D = 160, H = 30 nm, θ = 40°, and excited with a short-axis polarized source. (b) 3-D and 2-D cross-section views of the intensity distributions of the crescent at the λ = 270 and 530 nm resonances. The 2-D cross-section views are at the plane of the metal−substrate interface.

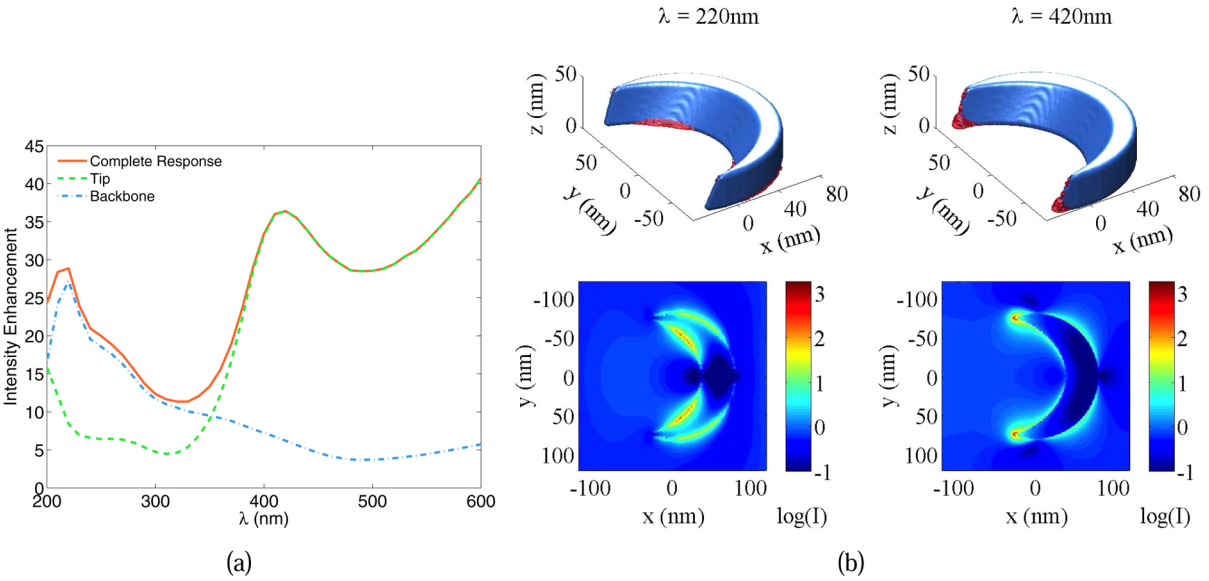

Figure 6. (a) Intensity enhancement response of crescent with D = 160 nm, H = 30 nm, and θ = 40°, and excited with a long-axis polarized source. (b) 3-D and 2-D cross-section views of the intensity distributions of the crescent at the λ = 220 and 420 nm resonances. The 2-D cross-section views are at the plane of the metal−substrate interface.

expected. Figure 7a shows that, when excited with a short-axis polarized source, the dipole resonance can be brought into the UV range by reducing the diameter to approximately 40 nm. For comparison, Figure 7d shows that, while the long-axis dipole resonance lies outside the plotted wavelength range, the quadrupole resonance can be blue-shifted into the UV range with diameters less than approximately 120 nm when using a deposition angle of 40°. Shift of the higher-order long-axis resonances as a function of diameter is also apparent, but the shift is more pronounced as a function of the deposition angle, as will be shown next.

Scaling with Deposition Angle. The backbone width of the crescent can be controlled by changing the deposition angle as described previously. The result of varying the deposition angle for short and long-axis polarized sources is shown in Figure 8a and b, respectively. Figure 8a shows that as the deposition angle is increased, the short-axis dipole resonance does undergo some blueshift. A similar response is observed in Figure 8b for the long-axis quadrupole resonance, with the greatest change occurring between 20 and 30° deposition angles in both cases.

The behavior of the higher-order resonances in general is to redshift with increasing deposition angle, which follows intuition since the backbone width increases with angle. However, as the backbone width increases, the inner and outer path lengths along the crescent decrease and increase, respectively, to the point that the higher-order resonances undergo splitting, as shown prominently for the short-axis polarization at θ = 60°. The local intensity patterns for these two modes are shown in Figure 9, showing that the shorter-

dx.doi.org/10.1021/ph400151n | ACS Photonics 2014, 1, 496−506

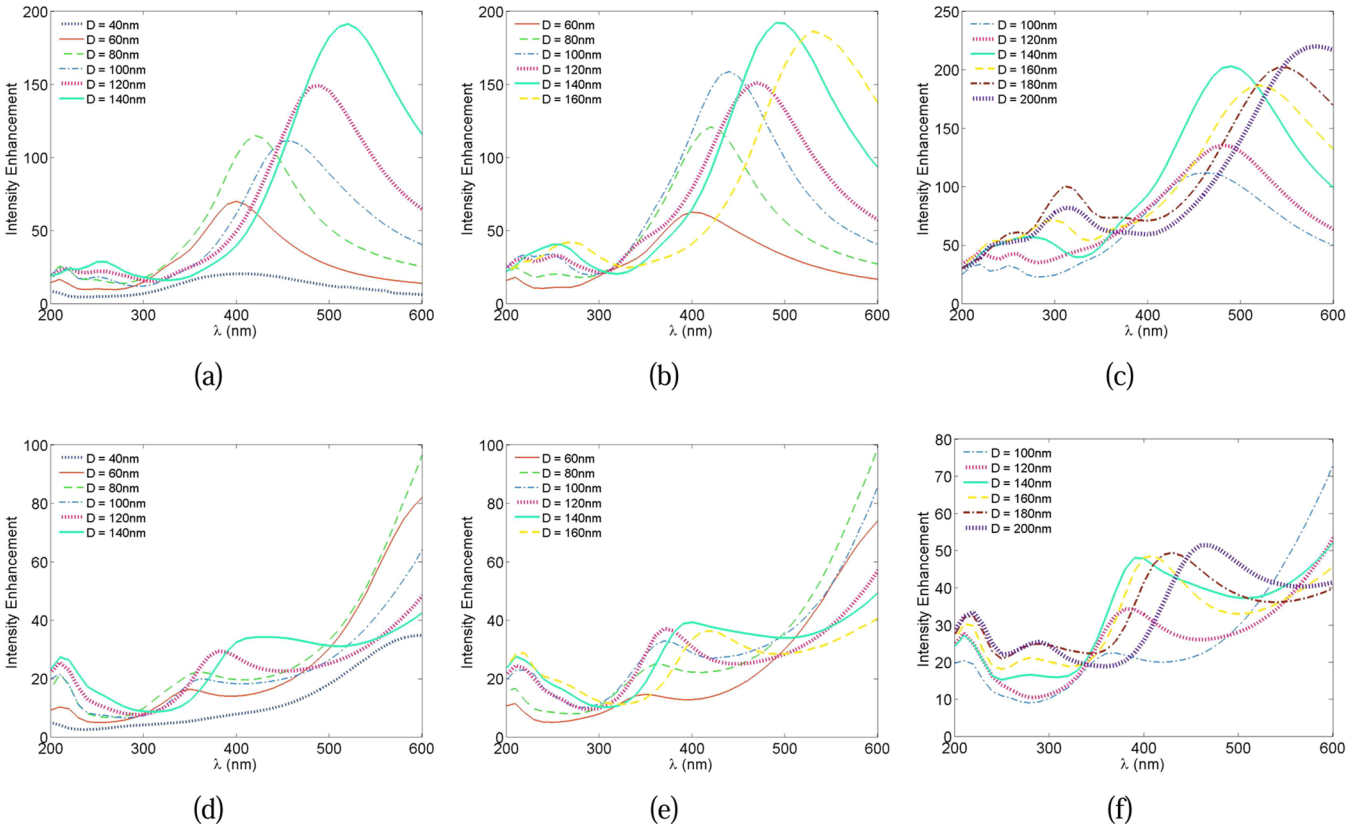

Figure 7. Near-field response of crescent antennas with (a, d) H = 20, (b, e) 30, and (c, f) 50 nm and θ = 40°, as the diameter is varied when excited by (a, b, c) short- and (d, e, f) long-axis polarized sources.

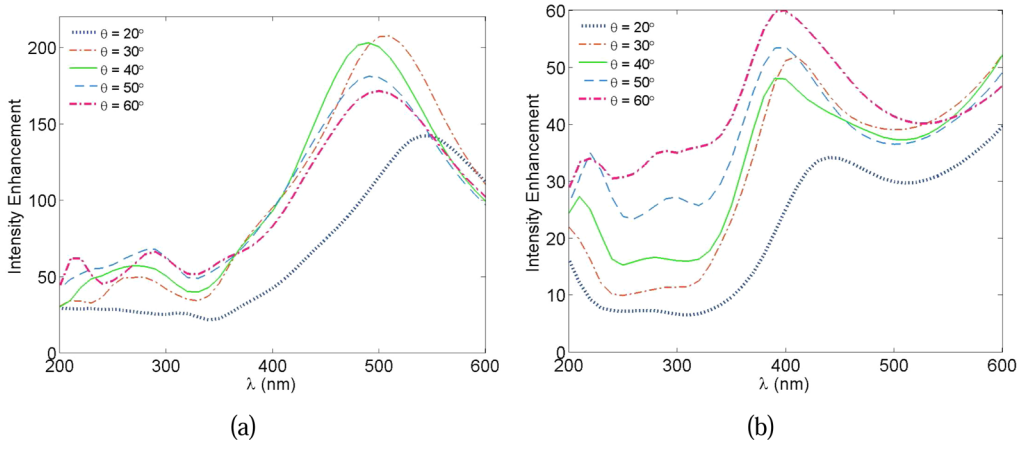

Figure 8. Near-field response of crescent with D = 140 nm and H = 50 nm as the deposition angle is varied when excited by (a) short- and (b) long-axis polarized sources.

wavelength mode has additional field nulls along the outside arc of the structure, Figure 9a,d, as compared to uniform intensity in Figure 9e. Comparing Figure 9 and Figure 5, the short-axis dipole and quadrupole modes remain relatively unchanged.

Similar behavior is seen for the long-axis resonance in the emergence of an additional higher-order mode for deposition angles $\theta \geq 40°$. For $\theta = 60°$, the two near-field intensity patterns are shown. At λ = 220 nm, Figure 10a,d, the intensity pattern is similar to that in Figure 6 (λ = 220 nm); however, a new intensity pattern emerges at the λ = 290 nm resonance wavelength, with intensity more localized at the tips (b, e). The intensity pattern at the long-axis quadrupole resonance (c, f) at λ = 400 nm is unchanged compared to Figure 6 at λ = 420 nm.

Scaling with Crescent Height. Crescent height has little effect in shifting the resonant wavelengths, but can be used as an optimizing parameter for intensity enhancement. Figure 11a for instance shows the intensity enhancement dependence on crescent height when a crescent with a diameter of 140 nm and a deposition angle of 40° is illuminated with a short axis polarized source. The figure shows that a crescent height of 50 nm results in the strongest dipole resonance, while a height of 70 nm results in the strongest quadrupole resonance.

Figure 11b shows the response for a long axis polarized source. Although the dipole resonance for this incident polarization occurs at much longer wavelengths, the quadrupole occurs within the wavelength range of interest and is maximized

dx.doi.org/10.1021/ph400151n | ACS Photonics 2014, 1, 496−506

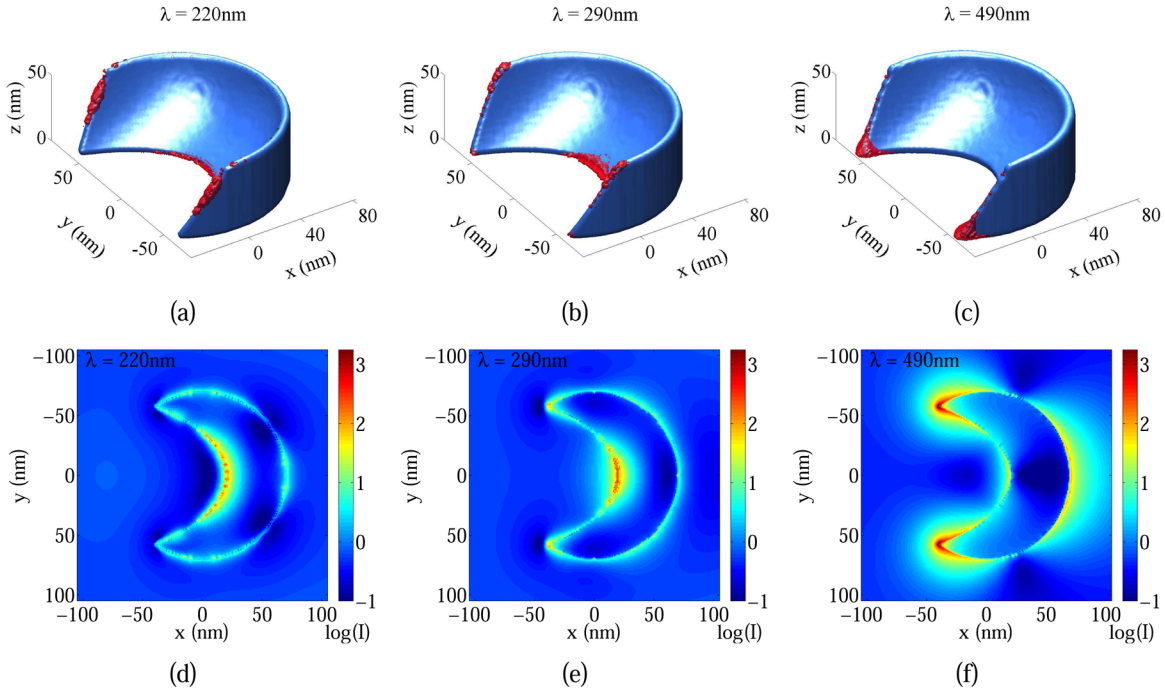

Figure 9. 3-D and 2-D cross-section views of the intensity distributions of a crescent antenna (D = 140 nm, H = 50 nm, $\theta = 60°$) at λ = 220, 290, and 490 nm under short-axis illumination. The 2-D cross-section views are at the plane of the metal−substrate interface.

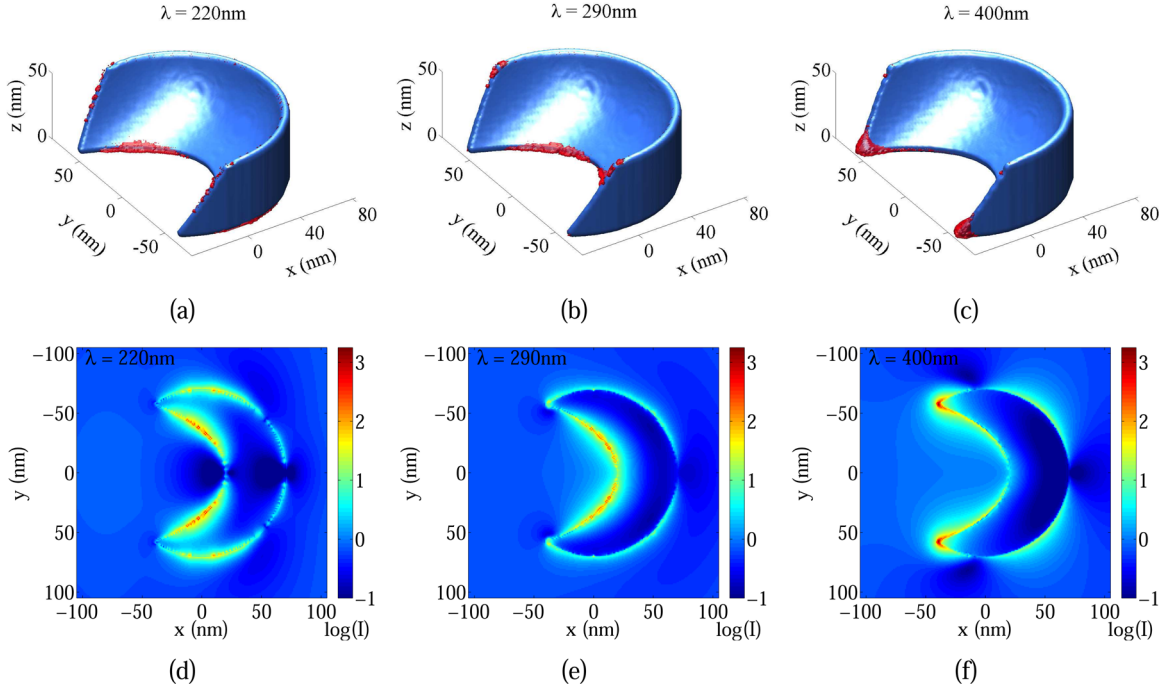

Figure 10. 3-D and 2-D cross-section views of the intensity distributions of a crescent antenna (D = 140 nm, H = 50 nm, $\theta = 60°$) at λ = 220, 290, and 400 nm under long-axis illumination. The 2-D cross-section views are at the plane of the metal−substrate interface.

with a height of 50 nm. The higher-order resonance at λ = 220 nm is maximized with a height of 60 nm.

Effect of Native Oxide Shell. Aluminum is an oxidizing metal, with the natural oxide thickness often quoted in the 2 to 3 nm range. The effect of this oxide layer on the plasmonic response of Al nanostructures has been studied by a number of groups.[10,11,29] A significant conclusion from these studies is that the presence of the oxide layer dampens and red-shifts the plasmonic response, especially when that response is due to highly localized fields, such as at tips or sharp corners. Aluminum oxide growth is self-terminating and is usually well-described by an inverse logarithmic law;[30,31] based on oxidation in an air environment at 295 K and 70% humidity, oxide thickness is about 2 nm after 24 h and reaches a steady-state thickness of about 2.5 nm after 10 days.[10,32]

It is not always feasible to maintain Al samples in a reduced oxygen environment or to perform measurements before significant oxidation occurs. There are situations, however, in

dx.doi.org/10.1021/ph400151n | ACS Photonics 2014, 1, 496−506

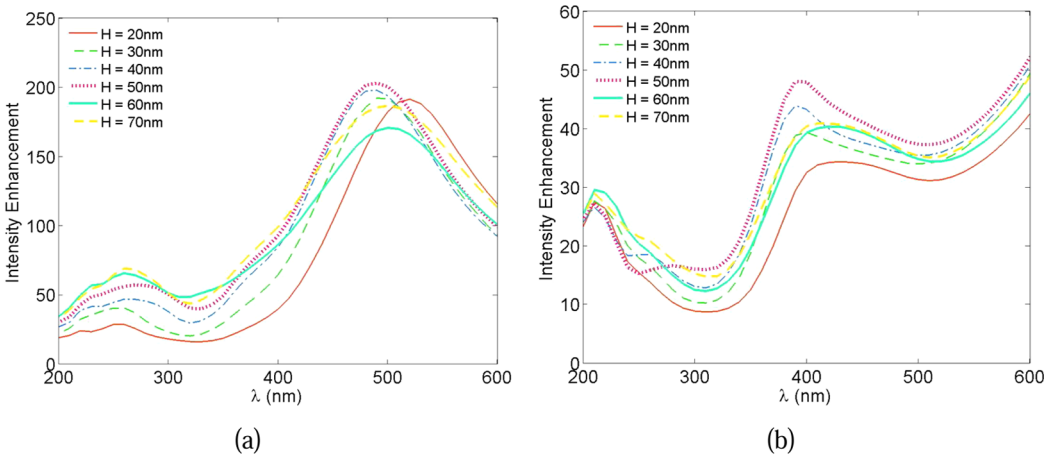

Figure 11. Near-field response of crescent with D = 140 nm and θ = 40° as the height is varied when excited by (a) short- and (b) long-axis polarized sources.

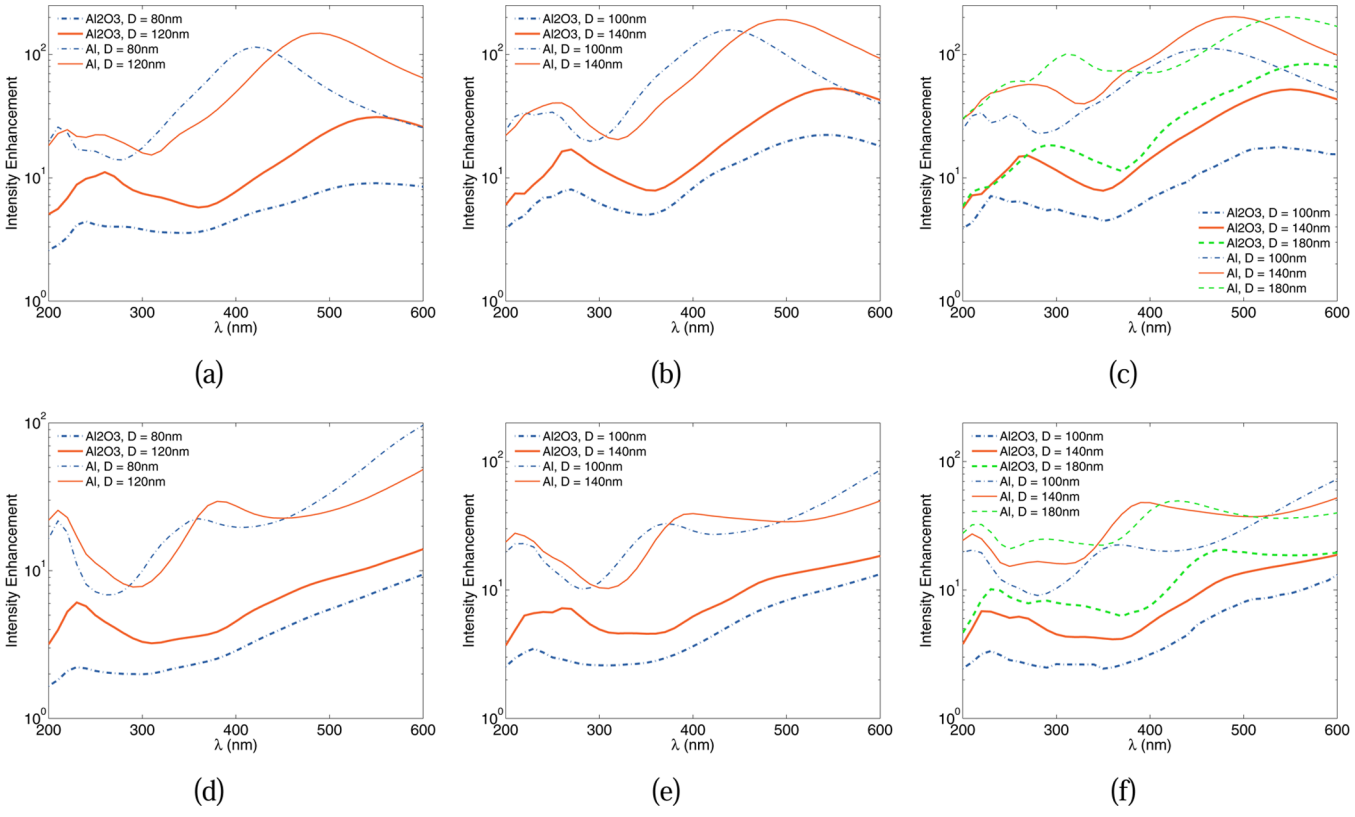

Figure 12. Near-field response of crescent antennas, including a 3 nm oxide shell, with (a, d) H = 20 nm, (b, e) H = 30 nm, (c, f) H = 50 nm, and θ = 40° as the diameter is varied when excited by (a–c) short- and (d–f) long-axis polarized sources. A log intensity scale is used to better exhibit the resonance peaks.

which neglecting the oxide layer, as represented by our results so far, may be a reasonable approximation. A number of surface passivation schemes have been developed that significantly reduce oxide growth, such as passivating with carboxylic acid,[33] an epoxide group,[34] or oleic acid.[35] Nevertheless, it is important to look at the effect of an oxide layer on nanocrescent antennas, as even a passivation process will produce a thin dielectric shell around the structure that could affect plasmonic response.

In the simulations to follow, the exposed surfaces of the nanocrescent structures were enclosed by a 3 nm shell of Al_2O_3. Due to numerical meshing considerations, the thickness was chosen to be a multiple of 1 nm, and 3 nm was chosen to slightly overestimate the effect. The structure model parameters D and H now reference the oxide shell, whereas the enclosed Al structure is correspondingly reduced in size. The reduction in size should blue-shift the plasmonic resonances, whereas the oxide shell (being of higher refractive index than the surrounding medium) should red-shift the resonances.

The effect of the oxide shell on the nanocrescent near-field resonances is shown in Figure 12 for different sizes D and H. Note that some of the smallest structures were not included in these results as their volume fractions of oxide resulted in negligible external intensity enhancement. In general, the resonances are red-shifted, with a reduction in intensity

dx.doi.org/10.1021/ph400151n | ACS Photonics 2014, 1, 496–506

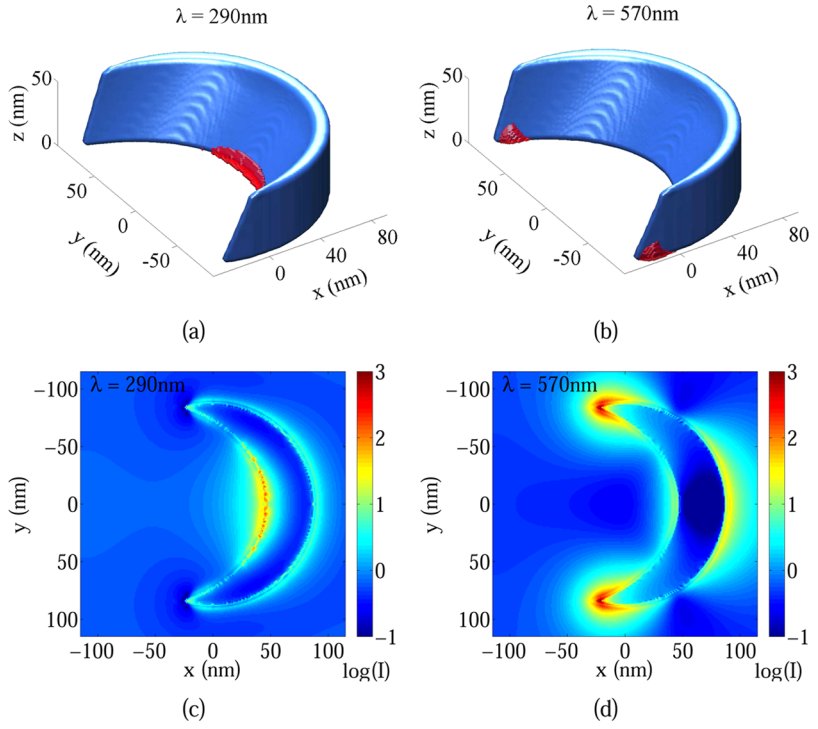

Figure 13. 3-D and 2-D cross-section views of the intensity distributions of a crescent antenna (D = 180 nm, H = 50 nm, $\theta = 40°$) with a 3 nm oxide shell, shown at λ = 290 and 570 nm under short-axis illumination. The 2-D cross-section views are at the plane of the metal−substrate interface.

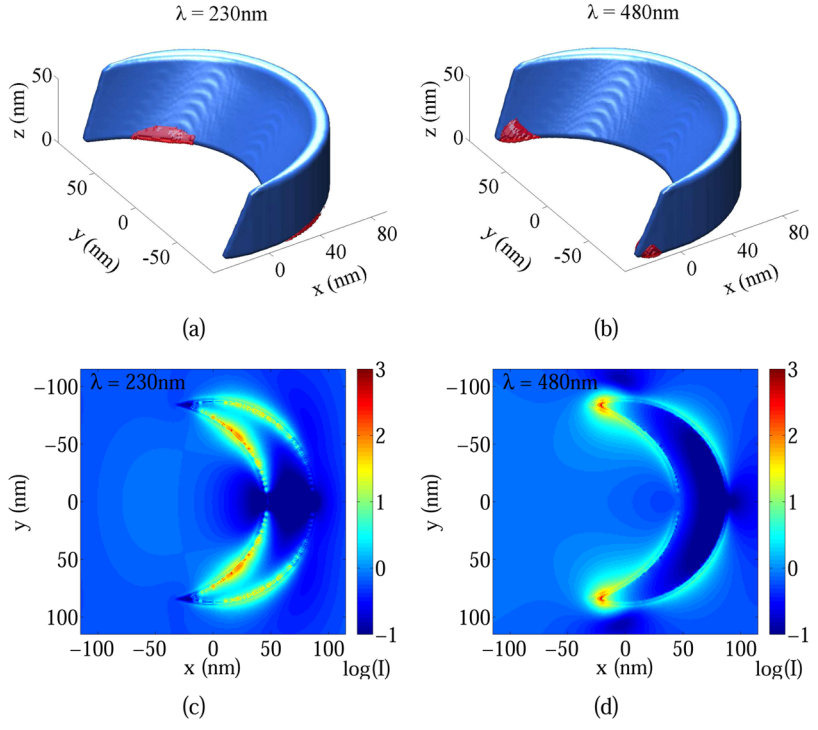

Figure 14. 3-D and 2-D cross-section views of the intensity distributions of a crescent antenna (D = 180 nm, H = 50 nm, $\theta = 40°$) with a 3 nm oxide shell, shown at λ = 230 and 480 nm under long-axis illumination. The 2-D cross-section views are at the plane of the metal−substrate interface.

measured outside of the structure. The significant reduction in intensity is primarily due to the fact that a portion of the enhanced local field is buried within the oxide layer. Thinner (e.g., H = 20 nm) and smaller (i.e., D < 100 nm) structures are more strongly affected. However, higher-order resonances of larger structures can still be utilized, with factor ∼10 enhancement achievable throughout the 200 to 400 nm range. As with the nonoxidized structures, some improvement in enhancement can be obtained by using greater deposition angles θ.

The effect of the oxide shell on the near-field intensity patterns is shown in Figures 13 and 14 for short- and long-axis illumination resonances, respectively. The 3-D renderings show the external intensity patterns, while the 2-D cross sections

dx.doi.org/10.1021/ph400151n | ACS Photonics 2014, 1, 496−506

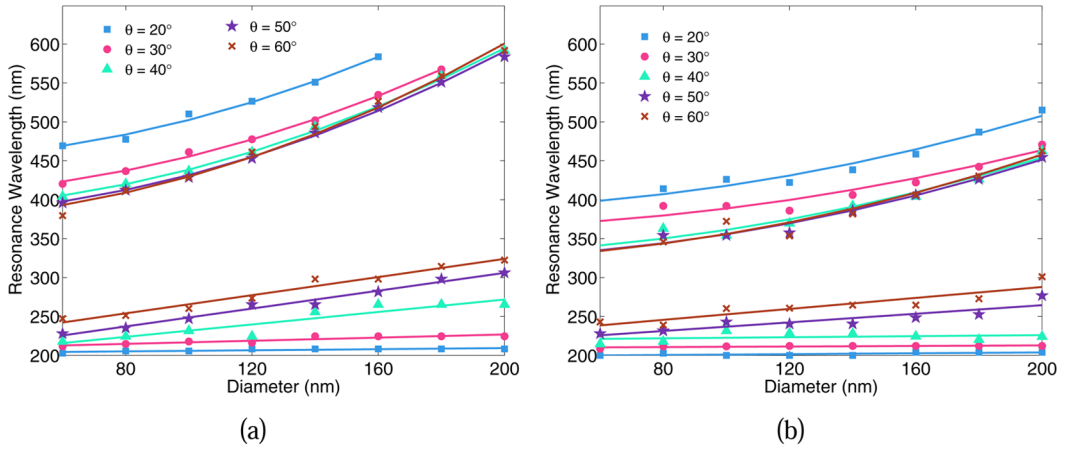

Figure 15. Nanocrescent resonances as the diameter is varied for different deposition angles with H = 30 nm when excited by (a) short- and (b) long-axis polarized sources. For short-axis excitation, positions of the dipole and quadrupole resonances are plotted. For long-axis excitation, positions of the quadrupole and principal higher-order resonances are plotted.

show the intensity patterns throughout the plane at the nanocrescent-substrate interface. In Figure 13d, the short-axis dipole mode pattern still exhibits strong field localization near the tips, but as shown in panel (b), the field that extends into the surrounding medium is split due to the increased effective oxide thickness at the tip apex, such that the region of strongest intensity enhancement is buried within the oxide shell. For the higher-order resonance at λ = 290 nm, Figure 13a,c, the enhancement pattern manifests primarily at the backbone interior, with peak external intensity enhancement values of about 30×.

Similar behaviors are seen for the long-axis resonances. Again, the highest near-field intensity at the tips for the quadrupole mode is buried within the oxide layer, as shown in Figure 14b,d, while the portion of the higher-order resonance mode at λ = 230 nm that extends into the surrounding medium is more strongly confined to the backbone region.

It should be noted that with the NTL fabrication method, scaling structure size requires $H \leq D/2$. It therefore appears to be infeasible to scale these structures small enough to access the short-axis dipole resonance in the UV due to dual effects of oxide formation: increasing oxide volume fraction and resonance red-shifting. The situation is similar for the long-axis quadrupole resonances and will generally be the case for the low-order resonances of any Al nanoantenna, especially antennas comprising tapered tips. However, local intensity enhancement in the UV can still be achieved through the higher-order resonance modes of larger nanocrescents, where these modes are localized in the backbone region and are less affected than the tips by geometrical curvature that increase the effective oxide thickness near the regions of highest enhancement.

CONCLUSIONS

Using a "UV plasmonic" metal such as aluminum, the response of nanocrescent antennas can be shifted to short wavelengths by appropriate manipulation of fabrication parameters, such as the angle of deposition, metal thickness and bead template diameter. Short-axis dipole and long-axis quadrupole resonances can be shifted into the UV range by using small diameters (Figure 15), but as the diameter decreases, so does local intensity enhancement. Higher-order modes, however, are very promising for operating in this range and can produce strong and tunable intensity enhancement. For a given diameter, the wavelength of operation of the short-wavelength resonances can be adjusted by using an appropriate angle of deposition (Figure 15) and the intensity enhancement can be adjusted through the height (Figure 11), neither of which present a restrictive change in the fabrication process.

For comparison, other investigations of the near-field response of UV antennas have been performed. A previous study of 40 nm diameter Al hemispheres predicted a ∼10× spatially averaged intensity enhancement (with a maximum enhancement of 200), also neglecting the native oxide layer.[36] The same study showed that, for the case of a spherical Al particle, corresponding enhancements are about 10× lower. Other studies have investigated local field enhancement in the gap between Al nanosphere dimers. Using 20 nm diameter Al spheres with a 1 nm gap, average gap enhancements ∼1000× were predicted throughout the UV.[22] Similar enhancements were predicted with 80 nm Al spheres and 2−8 nm gaps in the near-UV range.[37] Under the same assumption of neglecting the native oxide, the enhancements produced by the higher-order resonances of the nanocrescent are comparable: >50× spatially averaged intensity enhancement, with peak values ∼100×.

We further investigated the effect of the native oxide on the near-field response of the nanocrescent antenna. The presence of the oxide layer red shifts the near-field resonances and reduces the local intensity enhancement. Resonance modes with intensity localization near the tips are most strongly affected, making a stronger case for the use of higher-order resonances for UV response. Through the higher-order modes, averaged intensity enhancements >10× can still be achieved throughout the UV, with peak values of about 30×. Again, this is comparable to other reports. A previous study of ∼100 nm conical Al nanoparticles, incorporating a 3 nm oxide layer, predicted 100× peak enhancement in the mid-UV due to a quadrupolar resonance, with spatially averaged enhancement of ∼10× estimated from SERRS measurements.[38] A number of experimental fluorescence studies have also been performed, with typical enhancements ∼10× reported.[37,39]

In summary, we have shown that higher-order resonance modes of the nanocrescent produce a number of local intensity pattern combinations between the tips and backbone of the structure in the UV range. These modes can potentially be

dx.doi.org/10.1021/ph400151n | ACS Photonics 2014, 1, 496−506

exploited for applications in single-molecule spectroscopy and initiating localized photochemical reactions.

AUTHOR INFORMATION

Corresponding Author

*E-mail: blair@ece.utah.edu.

Notes

The authors declare no competing financial interest.

ACKNOWLEDGMENTS

This work was supported by NSF MRSEC grant DMR 1121252. M.R. also acknowledges support from NSF IGERT 0903715. We thank the reviewers for their helpful suggestions.

REFERENCES

(1) Bukasov, R.; Shumaker-Parry, J. S. Silver Nanocrescents with Infrared Plasmonic Properties As Tunable Substrates for Surface Enhanced Infrared Absorption Spectroscopy. *Anal. Chem.* **2009**, *81*, 4531−4535.

(2) Feng, L.; Van Orden, D.; Abashin, M.; Wang, Q.-J.; Chen, Y.-F.; Lomakin, V.; Fainman, Y. Nanoscale Optical Field Localization by Resonantly Focused Plasmons. *Opt. Express* **2009**, *17*, 4824−4832.

(3) Aubry, A.; Lei, D. Y.; Maier, S. A.; Pendry, J. B. Broadband Plasmonic Device Concentrating the Energy at the Nanoscale: The Crescent-Shaped Cylinder. *Phys. Rev. B* **2010**, *82*, 125430.

(4) Bukasov, R.; Ali, T. A.; Nordlander, P.; Shumaker-Parry, J. S. Probing the Plasmonic Near-Field of Gold Nanocrescent Antennas. *ACS Nano* **2010**, *4*, 6639−6650.

(5) Shumaker-Parry, J. S.; Rochholz, H.; Kreiter, M. Fabrication of Crescent-Shaped Optical Antennas. *Adv. Mater.* **2005**, *17*, 2131−2134.

(6) Bochenkov, V. E.; Sutherland, D. S. From Rings to Crescents: A Novel Fabrication Technique Uncovers the Transition Details. *Nano Lett.* **2013**, *13*, 1216−1220.

(7) Bukasov, R.; Shumaker-Parry, J. S. Highly Tunable Infrared Extinction Properties of Gold Nanocrescents. *Nano Lett.* **2007**, *7*, 1113−1118.

(8) Ray, K.; Chowdhury, M. H.; Lakowicz, J. R. Aluminum Nanostructured Films as Substrates for Enhanced Fluorescence in the Ultraviolet-Blue Spectral Region. *Anal. Chem.* **2007**, *79*, 6480−6487.

(9) Dörfer, T.; Schmitt, M.; Popp, J. Deep-UV Surface-Enhanced Raman Scattering. *J. Raman Spectrosc.* **2007**, *38*, 1379−1382.

(10) Langhammer, C.; Schwind, M.; Kasemo, B.; Zorić, I. Localized Surface Plasmon Resonances in Aluminum Nanodisks. *Nano Lett.* **2008**, *8*, 1461−1471.

(11) Chan, G. H.; Zhao, J.; Schatz, G. C.; Duyne, R. P. V. Localized Surface Plasmon Resonance Spectroscopy of Triangular Aluminum Nanoparticles. *J. Phys. Chem. C* **2008**, *112*, 13958−13963.

(12) Mahdavi, F.; Blair, S. Nanoaperture Fluorescence Enhancement in the Ultraviolet. *Plasmonics* **2010**, *5*, 169−174.

(13) Jiao, X.; Blair, S. Optical Antenna Design for Fluorescence Enhancement in the Ultraviolet. *Opt. Express* **2012**, *20*, 29909−29922.

(14) Li, L.; Fang Lim, S.; Puretzky, A. A.; Riehn, R.; Hallen, H. D. Near-Field Enhanced Ultraviolet Resonance Raman Spectroscopy Using Aluminum Bow-Tie Nano-Antenna. *Appl. Phys. Lett.* **2012**, *101*, −.

(15) Schwab, P. M.; Moosmann, C.; Wissert, M. D.; Schmidt, E. W. G.; Ilin, K. S.; Siegel, M.; Lemmer, U.; Eisler, H.-J. Linear and Nonlinear Optical Characterization of Aluminum Nanoantennas. *Nano Lett.* **2013**, *13*, 1535−1540.

(16) Sigle, D. O.; Perkins, E.; Baumberg, J. J.; Mahajan, S. Reproducible Deep-UV SERRS on Aluminum Nanovoids. *J. Phys. Chem. Lett.* **2013**, *4*, 1449−1452.

(17) Maidecchi, G.; Gonella, G.; Proietti Zaccaria, R.; Moroni, R.; Anghinolfi, L.; Giglia, A.; Nannarone, S.; Mattera, L.; Dai, H.-L.; Canepa, M.; Bisio, F. Deep Ultraviolet Plasmon Resonance in Aluminum Nanoparticle Arrays. *ACS Nano* **2013**, *7*, 5834−5841.

(18) Knight, M. W.; Liu, L.; Wang, Y.; Brown, L.; Mukherjee, S.; King, N. S.; Everitt, H. O.; Nordlander, P.; Halas, N. J. Aluminum Plasmonic Nanoantennas. *Nano Lett.* **2012**, *12*, 6000−6004.

(19) Zhou, L.; Gan, Q.; Bartoli, F. J.; Dierolf, V. Direct Near-Field Optical Imaging of UV Bowtie Nanoantennas. *Opt. Express* **2009**, *17*, 20301−20306.

(20) Ghenuche, P.; Cherukulappurath, S.; Taminiau, T. H.; van Hulst, N. F.; Quidant, R. Spectroscopic Mode Mapping of Resonant Plasmon Nanoantennas. *Phys. Rev. Lett.* **2008**, *101*, 116805.

(21) Cooper, C. T.; Rodriguez, M.; Blair, S.; Shumaker-Parry, J. S. Polarization Anisotropy of Multiple Localized Plasmon Resonance Modes in Noble Metal Nanocrescents. *J. Phys. Chem. C* **2014**, *118*, 1167−1173.

(22) McMahon, J. M.; Schatz, G. C.; Gray, S. K. Plasmonics in the Ultraviolet with the Poor Metals Al, Ga, In, Sn, Tl, Pb, and Bi. *Phys. Chem. Chem. Phys.* **2013**, *15*, 5415−5423.

(23) Aslan, K.; Previte, M. J. R.; Zhang, Y.; Geddes, C. D. Surface Plasmon Coupled Fluorescence in the Ultraviolet and Visible Spectral Regions Using Zinc Thin Films. *Anal. Chem.* **2008**, *80*, 7304−7312.

(24) Blaber, M. G.; Arnold, M. D.; Ford, M. J. A Review of the Optical Properties of Alloys and Intermetallics for Plasmonics. *J. Phys.: Condens. Matter* **2010**, *22*, 143201.

(25) Wu, P. C.; Kim, T.-H.; Suvorova, A.; Giangregorio, M.; Saunders, M.; Bruno, G.; Brown, A. S.; Losurdo, M. GaMg Alloy Nanoparticles for Broadly Tunable Plasmonics. *Small* **2011**, *7*, 751−756.

(26) Akbay, N.; Mahdavi, F.; Lakowicz, J. R.; Ray, K. Metal-Enhanced Intrinsic Fluorescence of Nucleic Acids Using Platinum Nanostructured Substrates. *Chem. Phys. Lett.* **2012**, *548*, 45−50.

(27) Appusamy, K.; Blair, S.; Nahata, A.; Guruswamy, S. Low-Loss Magnesium Films for Plasmonics. *Mater. Sci. Eng., B* **2014**, *181*, 77−85.

(28) Nanoparticle Scattering, 2013; https://www.lumerical.com/tcad-products/fdtd/applications/fdtd_nanoparticalnanoparticle_plasmon_cross_section.html.

(29) Knight, M. W.; King, N. S.; Liu, L.; Everitt, H. O.; Nordlander, P.; Halas, N. J. Aluminum for Plasmonics. *ACS Nano* **2013**, *8*, 834−840.

(30) Cabrera, N.; Mott, N. F. Theory of the Oxidation of Metals. *Rep. Prog. Phys.* **1949**, *12*, 163−184.

(31) Do, T.; McIntyre, N. S. Pressure Effects on Aluminium Oxidation Kinetics Using X-ray Photoelectron Spectroscopy and Parallel Factor Analysis. *Surf. Sci.* **1999**, *440*, 438−450.

(32) Piao, H.; Suominen Fuller, M.; Miller, D.; McIntyre, N. S. A Study of Thin Film Au-Al Alloy Oxidation in Ambient Air by X-ray Photoelectron Spectroscopy (XPS), X-ray Absorption Near Edge Structure (XANES), and Secondary Ion Mass Spectrometry (SIMS). *Appl. Surf. Sci.* **2002**, *187*, 266−274.

(33) Meziani, M. J.; Bunker, C. E.; Lu, F.; Li, H.; Wang, W.; Guliants, E. A.; Quinn, R. A.; Sun, Y.-P. Formation and Properties of Stabilized Aluminum Nanoparticles. *ACS Appl. Mater. Interfaces* **2009**, *1*, 703−709.

(34) Chung, S. W.; Guliants, E. A.; Bunker, C. E.; Hammerstroem, D. W. .; Deng, Y.; Burgers, M. A.; Jelliss, P. A.; Buckner, S. W. . Capping and Passivation of Aluminum Nanoparticles Using Alkyl-Substituted Epoxides. *Langmuir* **2009**, *25*, 8883−8887.

(35) Lee, H. M.; Yun, J.-Y. Preparation of Aluminum-oleic Acid Nanocomposite for Application to Electrode for Si Solar Cells. *Mater. Trans.* **2011**, *52*, 1222−1227.

(36) Sanz, J. M.; Ortiz, D.; Alcaraz de la Osa, R.; Saiz, J. M.; González, F.; Brown, A. S.; Losurdo, M.; Everitt, H. O.; Moreno, F. UV Plasmonic Behavior of Various Metal Nanoparticles in the Near- and Far-Field Regimes: Geometry and Substrate Effects. *J. Phys. Chem. C* **2013**, *117*, 19606−19615.

(37) Chowdhury, M. H.; Ray, K.; Gray, S. K.; Pond, J.; Lakowicz, J. R. Aluminum Nanoparticles As Substrates for Metal-Enhanced Fluorescence in the Ultraviolet for the Label-Free Detection of Biomolecules. *Anal. Chem.* **2009**, *81*, 1397−1403.

(38) Jha, S. K.; Ahmed, Z.; Agio, M.; Ekinci, Y.; Löffler, J. F. Deep-UV Surface-Enhanced Resonance Raman Scattering of Adenine on Aluminum Nanoparticle Arrays. *J. Am. Chem. Soc.* **2012**, *134*, 1966−1969.
(39) Chowdhury, M. H.; Chakraborty, S.; Lakowicz, J. R.; Ray, K. Feasibility of Using Bimetallic Plasmonic Nanostructures to Enhance the Intrinsic Emission of Biomolecules. *J. Phys. Chem. C* **2011**, *115*, 16879−16891.